Chemical Science

Accepted Manuscript

This article can be cited before page numbers have been issued, to do this please use: S. GRATIOUS, B. Li, D. Mondal, D. A. Varghese, A. Kumar, J. Thomas, D. Jiang, V. B. Kamble and S. Mandal, *Chem. Sci.*, 2025, DOI: 10.1039/D5SC02515J.




ROYAL SOCIETY OF CHEMISTRY

rsc.li/chemical-science

View Article Online
DOI: 10.1039/D5SC02515J

ARTICLE

# Identifying the Superatomic $AuCu_{56}$ Nanocluster through a Ligand-exchange Coupled Metal-exchange Induced Transformation

Received 00th January 20xx,
Accepted 00th January 20xx

DOI: 10.1039/x0xx00000x

*Saniya Gratious,[a] Bo Li,[b] Dipanjana Mondal,[c] Alok Kumar,[a] Dayona Aleyamma Varghese,[a] Jibin Thomas,[a] De-en Jiang,[b]* Vinayak Kamble,[c] Sukhendu Mandal[a]**

Quantum-sized metal nanoclusters can be viewed as superatoms that mimic the electron-shell closing behaviours of atoms, where these electronic shell configurations often govern their properties. Various superatomic nanoclusters with diverse structures and valence states have been identified over the past few years, but the 1S valence state of atomically precise Au nanoclusters have rarely been seen. Herein, we have achieved the synthesis of a $1S^1$ superatomic $[AuCu_{56}S_{12}(SAdm)_{20}(O_3SAdm)_{12}]$ nanocluster from the eight-electron $[Au_{23}(S\text{-}c\text{-}C_6H_{11})_{16}]^-$ nanocluster *via* a ligand-exchange coupled metal-exchange induced transformation. Detailed studies through mass spectrometry provided insights into the nanocluster formation, and theoretical studies revealed the superatomic nature of the nanocluster. Moreover, the as-synthesized nanocluster exhibited a broad optical absorption, leading to good photocurrent response under UV illumination. This work introduces a novel doping strategy that enables us to realize a rare superatomic valence state in an alloy cluster and to explore its unique light-induced properties.

## Introduction

Atomically precise metal nanoclusters (NCs) have garnered substantial interest in recent years due to their extraordinary stability and intriguing physicochemical properties, with recent examples like an all-metal fullerene, $[K@Au_{12}Sb_{20}]^{5-}$ highlighting their expanding structural diversity.[1–5] Moreover, the ability of these NCs to mimic the properties of single atoms identifies them as "superatoms", where the superatomic core is stabilized by protecting ligands.[6–8] Analogous to the atomic theory, the "superatomic theory" also explains the stability and nature of these metal NCs, which are based on the guiding rules of compact geometry and electronic shell closing.[6] A well-studied example is the thiolate-protected $[Au_{25}(SR)_{18}]^-$ NC, which has an $Au_{13}$ icosahedral core with three pairs of $Au_2(SR)_3$ staple motifs protecting the inner core. The exceptional stability of this $[Au_{25}(SR)_{18}]^-$ NC was explained by its closed-shell electronic configuration of $1S^21P^6$.[9] Several other superatomic NCs with various valence electron counts and diverse structures were also identified over the past few decades.[10–16] However, the guiding principles regarding the evolution of superatomic NCs as a function of their atomic arrangement have not yet been achieved. According to the superatom model, both the core composition and the surrounding ligands contribute towards the electronic stability of ligand protected NCs.[17–21] Hence, the manipulation of the photophysical properties of these superatomic NCs can be achieved by core or surface engineering.

Transformation chemistry has served as a versatile approach to manipulate the core and surface structures of atomically precise metal NCs and access novel NCs with diverse structures and intriguing properties.[22–25] Several methods of transformation have been developed over time, where the metal-exchange and ligand-exchange induced size/structure transformation have prevailed as superior techniques to tune the core and surface composition of metal NCs.[26–28] The metal-exchange induced size/structure transformation (MEIST) helps in understanding the doping effects on electronic structures and physicochemical properties of NCs[22,25–27], whereas, the ligand-exchange induced size/structure transformation (LEIST) helps in understanding the effects of surface modulation.[27,29–32] To date, there are various examples of MEIST[33–45] and LEIST[29,46–50] reported on atomically precise NCs, however, the combined effect of both MEIST and LEIST on the structural growth patterns and corresponding property evolution of NCs is not yet explored. This gap in knowledge demands the need for a thorough mechanistic study of these two techniques to advance the alloy NC library and understand their electronic and geometric structure evolution.

In this regard, we present a novel doping strategy that integrates both the ligand-exchange and metal-exchange methods on the eight-electron $[Au_{23}(S\text{-}c\text{-}C_6H_{11})_{16}]^-$ NC.[51] Investigations through time-dependent mass spectrometry underscored the occurrence of LEIST followed by MEIST on the precursor $[Au_{23}(S\text{-}c\text{-}C_6H_{11})_{16}]^-$ NC. Single-crystal X-ray diffraction (SCXRD) studies revealed the formation of an $[AuCu_{56}S_{12}(SAdm)_{20}(O_3SAdm)_{12}]$ (in short, $AuCu_{56}$) NC with an Au in

[a] School of Chemistry, Indian Institute of Science Education and Research Thiruvananthapuram, Kerala 695551, India. E-mail: sukhendu@iisertvm.ac.in
[b] Department of Chemical and Biomolecular Engineering, Vanderbilt University, Nashville, TN 37235 USA. E-mail: de-en.jiang@vanderbilt.edu
[c] School of Physics, Indian Institute of Science Education and Research Thiruvananthapuram, Kerala 695551, India.
†Electronic Supplementary Information (ESI) available. See DOI: 10.1039/x0xx00000x

the inner core. The theoretical calculations provided insights into the superatomic nature of the $AuCu_{56}$ NC with an electronic configuration of $1S^1$. This newly synthesized doped $AuCu_{56}$ NC exhibited good photocurrent response upon UV irradiation, with fast response and recovery times. This study not only enhances our understanding of the evolution of the electronic and geometric structure of superatomic bimetallic NC but also paves the way for new applications and further exploration in the field of alloy NCs.

## Results and Discussion

**Scheme 1. Synthesis of the $AuCu_{56}$ NC from $[Au_{23}(S\text{-}c\text{-}C_6H_{11})_{16}]^-$ NC.**

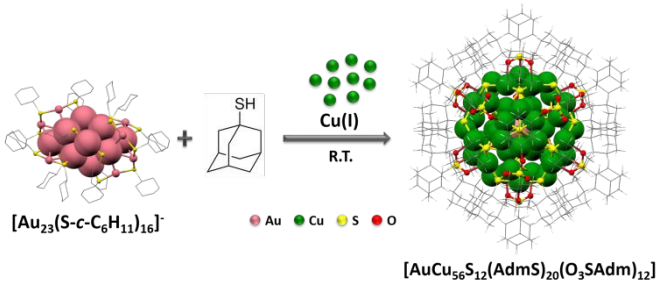


**Synthesis of the $AuCu_{56}$ Nanocluster.** The synthesis of $AuCu_{56}$ was achieved *via* the ligand-exchange induced size/structure transformation (LEIST) followed by metal-exchange of the $[Au_{23}(S\text{-}c\text{-}C_6H_{11})_{16}]^-$ (hereafter, $Au_{23}$) NC. The $Au_{23}$ NC was synthesized and characterized by following the reported procedure.[51] The characteristic peak at 570 nm and the shoulder peak at 460 nm in the UV-vis absorption spectrum matched with the reported spectrum (**Fig. S1a**). The matrix-assisted laser desorption ionization mass spectrometry (MALDI-MS) data showed a single peak at m/z = 6373.13 corresponding to the molecular-ion peak of the intact $Au_{23}$ NC (**Fig. S1b**). The transformation reaction was carried out by the addition of 1-adamantanethiol to the molecularly pure $Au_{23}$ NC in DCM, followed by the addition of $Cu(CH_3CN)_4(BF_4)$ dissolved in $CH_3CN$ (more information can be found in the SI). The transformation reaction was monitored through time-dependent UV-vis and MALDI-MS studies by taking aliquots from the reaction mixture at regular intervals. The UV-vis absorption spectra at the beginning of the reaction showed characteristic features of $Au_{23}$ NC, however in the presence of excess 1-adamantanethiol and Cu(I) salt, the absorption spectrum became almost featureless with weak absorption around 500 nm **(Fig. S2)**, which remained the same throughout the reaction. Time-dependent mass spectrometric studies of the aliquots were also carried out using MALDI-MS. At the beginning of the reaction (0 min), an intense peak at m/z = 6373.13 was observed, which corresponds to the intact $[Au_{23}(S\text{-}c\text{-}C_6H_{11})_{16}]^-$ NC **(Fig. S3)**. However, within 1 min of the addition of excess 1-adamantanethiol to the reaction mixture, peaks started appearing at m/z = 6488.30, 6175.82, 5863.96, which corresponds to $[Au_{23}(S\text{-}c\text{-}C_6H_{11})_{17}]$, $[Au_{22}(S\text{-}c\text{-}C_6H_{11})_{16}]$, and $[Au_{21}(S\text{-}c\text{-}C_6H_{11})_{15}]$, respectively. As time proceeds, these three peaks, along with a new peak at m/z = 6800.71 corresponding to $[Au_{24}(S\text{-}c\text{-}C_6H_{11})_{18}]$, indicate ligand-exchange with 1-adamantanethiol, which is evident from the formation of a new set of peaks with an equal spacing of 52 Da (difference between incoming adamantanethiol and existing cyclohexanethiol) **(Table S1)**. Subsequently, after 2 min, the Cu(I) salt was added to the reaction mixture, which entirely changed the mass spectral profile, and several new peaks were observed in the range of m/z = 4500 - 6500 **(Fig. S4)**. As the reaction advances, this broad range of peaks gradually narrowed to 5000 - 6000 m/z and further evolved into two sets of peaks ranging from m/z = 5000 - 6000 and m/z = 6000 - 7000 by the end of 2 h. We have carried out Electrospray Ionization mass spectrometry (ESI-MS) analysis of the aliquots at lower mass ranges **(Fig. S5)**, which showed peaks with a spacing of 133 Da corresponding to the difference between Au and Cu. This is attributed to the metal-exchange taking place during the transformation reaction. Hence, it can be inferred that the parent $Au_{23}$NC undergoes LEIST with adamanatanethiol, which

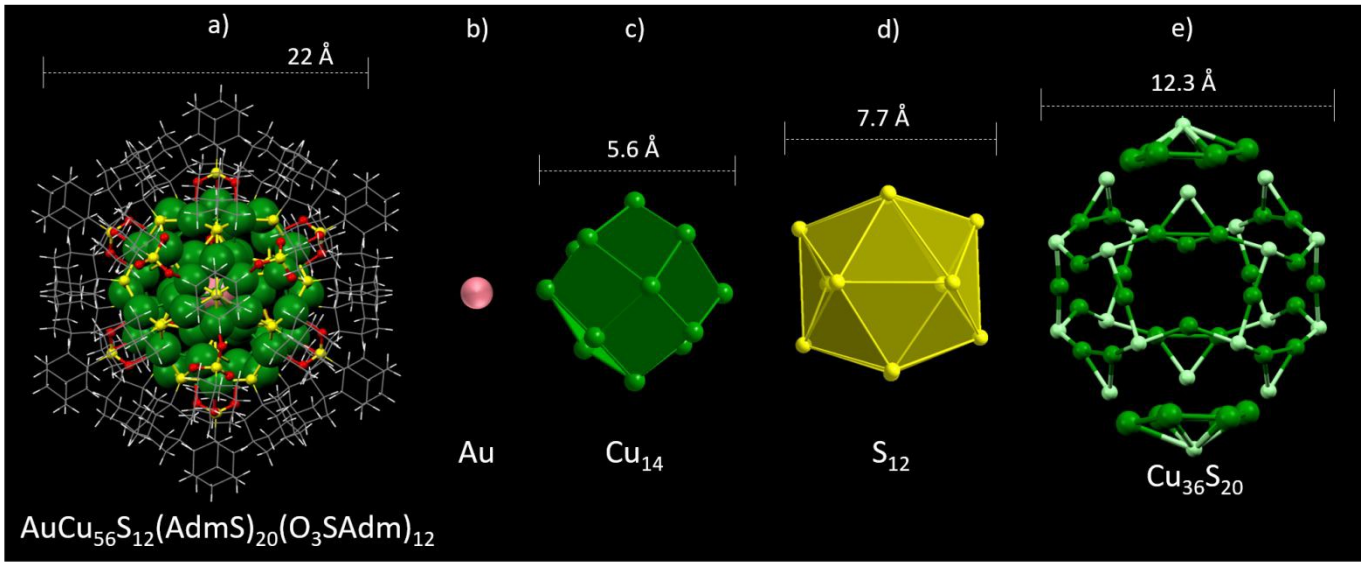


**Figure 1.** Overview of the atomic structure of the $AuCu_{56}$ NC. a) Total structure of the $AuCu_{56}$ NC. b) The innermost Au atom present inside the c) $Cu_{14}$ cuboactahedron which is then connected to d) a layer of 12 $S^{2-}$ arranged in the shape of an icosahedron. e) The atomic structure of the $Cu_{36}S_{20}$ outermost layer. Color code: pink, Au; green, Cu; yellow and light green, S; red, O; gray, C; white, H.

in turn undergoes the metal-exchange with Cu.

The reaction was allowed to proceed for 2 h at room temperature, which was then washed with MeOH and extracted with DCM to remove unreacted starting materials. Unique six-legged "stellate" crystals were grown by layering the DCM solution of the as-obtained product with hexane (**Fig. S6**) in three weeks (~10 % yield, Cu-atom basis).

**Crystal Structure Analysis.** The star-shaped crystals were analyzed using SCXRD, which revealed the molecular formula of the NC to be $[AuCu_{56}S_{12}(SAdm)_{20}(O_3SAdm)_{12}]$ (hereafter $AuCu_{56}$) with a space group of *Pa*-3 (205) **(Table S2)**. The $AuCu_{56}$ NC structure possesses a $C_3$ symmetry and is composed of one Au atom, 56 Cu atoms, 12 $S^{2-}$ ions, 20 adamantanethiolate ($C_{10}H_{15}S^-$) ligands, and 12 adamantane sulphonate ($C_{10}H_{15}SO_3^-$) ligands (**Fig. 1a**). The overall structure of the $AuCu_{56}$ can be visualized as an Au-centered double-shell copper framework, which is further protected by the thiolate ligands. This innermost Au atom (**Fig. 1b**) sourced from the $Au_{23}$ parent NC,

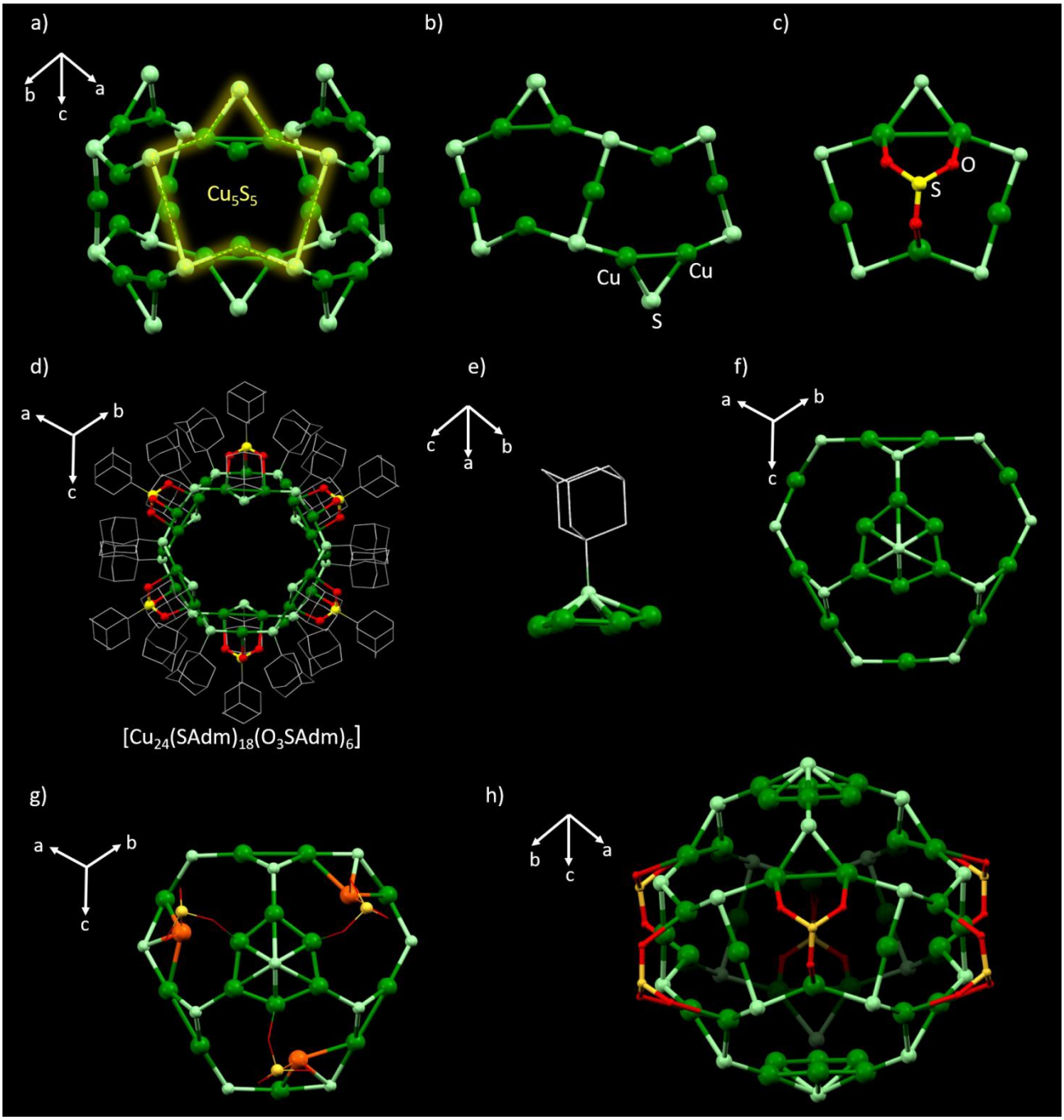


**Figure 2.** Structural details of the $AuCu_{56}$ NC. a) The outer $[Cu_{24}S_{18}]$ layer of the $AuCu_{56}$ NC. b) The $Cu_5S_5$ star motif pair of the $[Cu_{24}S_{18}]$ layer, c) binding of the adamantane sulphonate to the $Cu_5S_5$ star motif and d) the $[Cu_{24}S_{18}]$ layer with the adamantane moieties. e) The hexagonal $[Cu_6]$ unit capping the $[Cu_{24}S_{18}]$ layer and f) top view of its binding mode. g) Further connections between the $[Cu_{24}S_{18}]$ layer and the $[Cu_6]$ unit *via* three Cu atoms and finally the h) overall $[Cu_{36}S_{26}(SO_3)_6]$ outermost layer excluding the adamantane moieties. Color code: pink, Au; green and orange, Cu; yellow and light green, S; red, O; gray, C. Hydrogen atoms are omitted for clarity.

is surrounded by 14 Cu atoms arranged in the shape of a rhombic dodecahedron with 12 [$Cu_4$] faces (**Fig. 1c**). This $Cu_{14}$ inner core has an average Cu…Cu distance of 2.62 Å, which falls under the Cu...Cu Van der Waals interaction range of 2.8 Å. The presence of a hollow [$Cu_{14}$] core has been previously observed in a [S-$Cu_{50}$] NC, with similar bonding patterns.[52] However, this work reports a high nuclearity $AuCu_{56}$ NC with a single Au-centered core, which is energetically favorable than the hollow ones.[53] In-depth structural analysis revealed that each of the [$Cu_4$] face of the [$Cu_{14}$] core is capped by one $S^{2-}$ ion *via* $\mu^3$-bridging with an average Cu…S distance of 2.27 Å (**Fig. S7**). These 12 $S^{2-}$ ions are arranged in the shape of an icosahedron with no S-S bonds between them (**Fig. 1d**), and therefore cannot be considered as a separate shell (average S-S distance of 4.07 Å). This [$Au@Cu_{14}S_{12}$] shell is further protected by a [$Cu_{36}S_{20}$] layer (**Fig. 1e**), where these S atoms are a part of the adamantanethiol ligands. This outermost layer can be divided into a [$Cu_{24}S_{18}$] layer capped with two sets of [$Cu_6$] units at the top and the bottom. The [$Cu_{24}S_{18}$] layer can be viewed as an open-shell consisting of 3 pairs of [$Cu_5S_5$] star-like motifs arranged around the waist of the [$Au@Cu_{14}S_{12}$] shell (**Fig. 2a**). Each pair consists of two edge-sharing $Cu_5S_5$ stars with one motif facing upwards and the other downwards (**Fig. 2b**). Moreover, the inner $S^{2-}$ layer is bound to three Cu atoms from each star motif *via* $\mu^3$-bridging with an average Cu…S distance of 2.59 Å, showing an overall $\mu^6$-bridging pattern. The same three Cu atoms of each star motif are further capped by one adamantane sulphonate ligand (**Fig. 2c**) formed *in-situ* during the synthesis, yielding a total of 6 adamantane sulphonate ligands and 18 adamantanethiol ligands protecting the [$Cu_{24}S_{18}$] layer (**Fig. 2d**). The [$Cu_{24}S_{18}$] layer is capped by the hexagonal [$Cu_6$] units (**Fig. 2e**) through its three alternate Cu atoms to the three apex S atoms of the [$Cu_{24}S_{18}$] star motifs at the top and the bottom (**Fig. 2f**). This [$Cu_6$] units are further protected by adamantanethiol ligands, giving rise to a closed [$Cu_{36}S_{20}(O_3S)_6$] shell. The remaining six Cu atoms of the $AuCu_{56}$ NC connect this hexagonal [$Cu_6$] unit with the [$Cu_{24}S_{18}$] layer through adamantane sulphonate ligands with three at the top and three at the bottom in a $\eta^2$: $\eta^1$ fashion (**Fig. 2g**), forming the [$Cu_{42}S_{20}(O_3S)_6$] (**Fig. 2h**). An interesting observation here is that the only Cu atoms that are bound to the inner $S^{2-}$ layer bind to the adamantane sulphonate ligands in the outer layer. Every

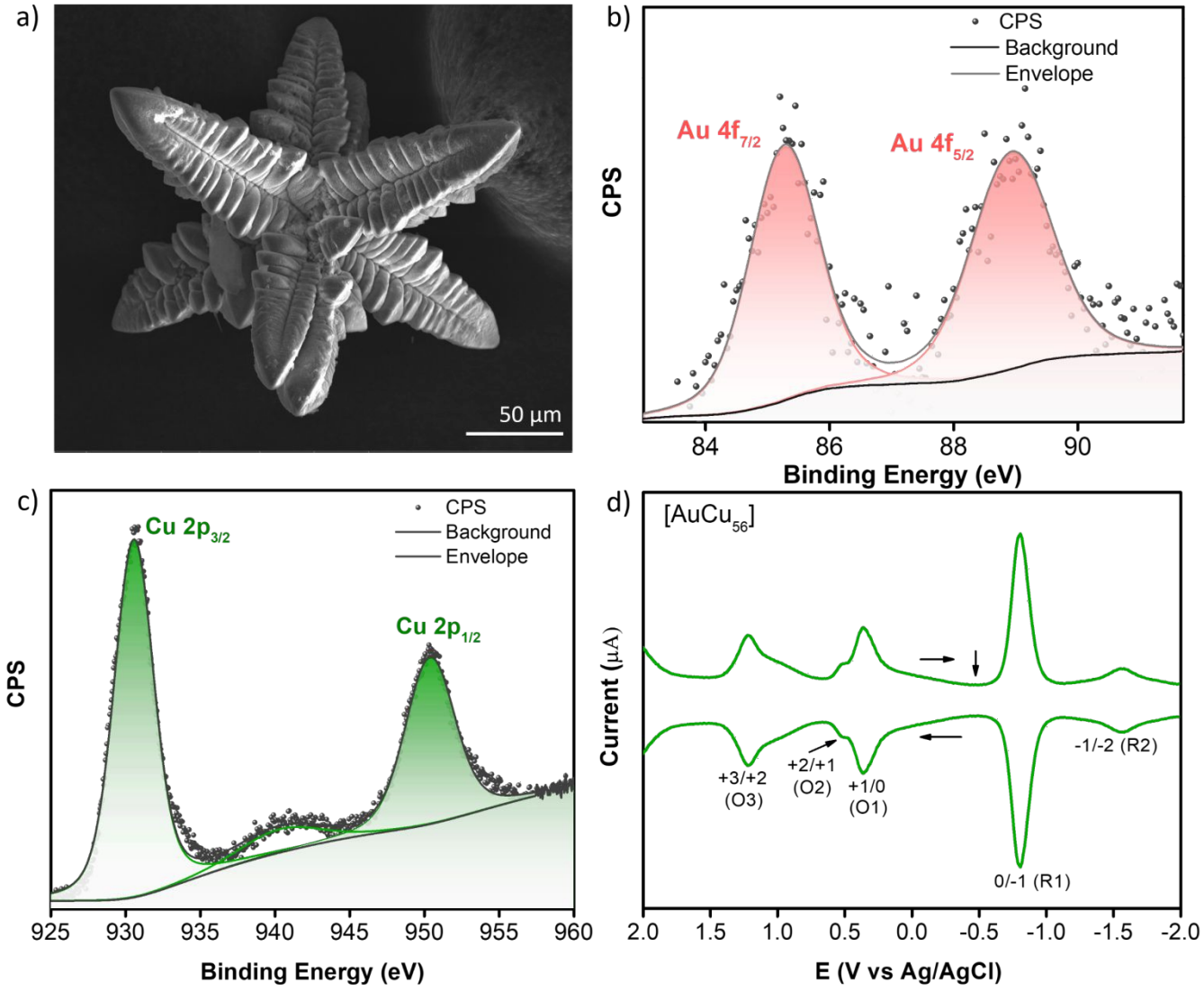


**Figure 3.** a) SEM image showing the star-shaped crystals with multiple branches. XPS spectra of the $AuCu_{56}$ NC showing the b) Au 4f and c) Cu 2p orbitals; d) Differential pulse voltammetry of [$AuCu_{56}S_{12}(AdmS)_{20}(O_3SAdm)_{12}$] NC at a GC electrode (15 mm). DC potential ramp of 10 mV/s and a pulse amplitude of 50 mV.

View Article Online
DOI: 10.1039/D5SC02515J



other Cu atom which only binds to the adamantanethiol ligands has no direct interaction with the inner $S^{2-}$ layer. This reveals the driving force for the *in-situ* oxidation of adamantanethiol ligands to give the adamantane sulphonate ligands.[54]

The $AuCu_{56}$ NC adopts a cubic geometry with each unit cell occupying twelve NCs at the edge centers and one at the body-center, making the effective number of molecules per unit cell 4 (**Fig. S8**). The unit cell follows an AB-type stacking where the packing mode is directed by the intermolecular CH…HC non-bonding interactions of length ~ 2.28 Å (**Fig. S9**). The previously reported [S-$Cu_{50}$] also exhibits a similar geometry, however, its packing mode is directed by C-H…F hydrogen bonding, which extends the cubic NCs to an overall cubic superstructure.[52] Whereas in this work, the intermolecular CH…HC interactions between the adamantane ligands act as the "sticky fingers" to extend the packing and give unique star-shaped crystals (**Fig. S6**).

**Characterizations.** The optical microscopic images of the $AuCu_{56}$ crystals showed blackish star-like crystals of ~ 500 µm diameter with multiple branches resembling a snowflake (**Fig. S6**). These crystals were characterized using Scanning Electron Microscopy (SEM) and Transmission Electron Microscopy (TEM) to understand their surface morphology and elemental composition. The SEM images showed a fern-like morphology for each of the branches with several terraces and steps on the surface (**Fig. 3a**). Several smaller branches were also observed to be originating from the center of the crystal. The TEM imaging of the crystals dispersed in MeOH showed a uniform distribution of spherical particles of size ~ 2.0 nm with little-to-no aggregation (**Figs. S10a, b**). The elemental analysis confirmed the presence of Au, Cu, S, and O in appropriate amounts (**Fig. S11**). X-ray photoelectron spectroscopy (XPS) was done to confirm the composition of the $AuCu_{56}$ NC **(Figs. 3b, c).** The Au4f XPS spectrum exhibited two broad peaks at 85.3 and 88.9 eV corresponding to the $Au4f_{7/2}$ and $Au4f_{5/2}$ spin-orbit components, respectively, which indicates a $Au^{\delta+}$ state of Au ($0 < \delta < +1$), in the inner core of the $AuCu_{56}$ NC (**Fig. 3b**).[55] The Cu XPS showed peaks at 930.5 eV and 950.3 eV corresponding to $Cu2p_{3/2}$ and $Cu2p_{1/2}$, respectively, with a significant split between the components, while a weak satellite peak was observed at ~ 943 eV, suggesting the Cu atoms present in the NC are predominantly in +1 oxidation state (**Fig. 3c**).[56] The presence of two oxidation states for S was observed in the XPS, which is consistent with the structure modelled from SCXRD. The S2p spectrum showed a prominent peak at 162.8 eV corresponding to the $S^{2-}$ state and a weaker peak at 168.2 eV corresponding to the $S^{5+}$ state from the adamantane sulphonate ligands (**Fig. S12a**). Deconvolution of these peaks revealed the corresponding spin-orbit components with a spacing of ~1.1 eV. The survey spectrum (**Fig. S12b**) shows the presence of all corresponding elements in the $AuCu_{56}$ NC.

To obtain a more comprehensive understanding of the electronic structures of the $AuCu_{56}$ NC, we carried out differential pulse voltammetry (DPV) measurements of the $AuCu_{56}$ NC (**Fig. 3d)**. In **Fig. S13**, the cyclic voltammograms and DPV are presented, where the blue vertical arrow highlights the first negative and positive redox peaks, and the horizontal arrow indicates the scanning direction. The clearly defined charging peaks are observed within the voltage range of -2 to +2 V. This phenomenon is attributed to the discrete charging of the NC at the electrode interface. This finding is indicative of the molecular-like electronic energy of the NC, which is influenced by the ultrasmall core dimension.[57] **Fig. 3d** illustrates the DPV of the NC measured across the same potential ranges. The peaks labelled O1, O2, and O3 correspond to the first, second, and third oxidation couples, respectively, while R1 and R2 represent the first and second reduction couples. An overview of these redox couples is provided in

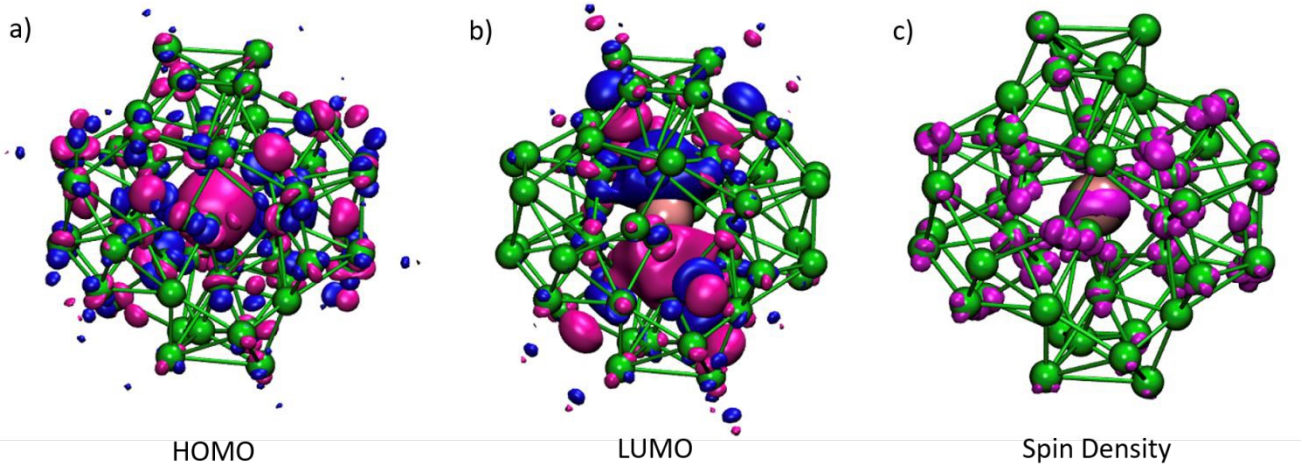


**Figure 4.** a) HOMO and b) LUMO (magenta and blue isosurfaces) and c) spin density (magenta isosurfaces) of the DFT-optimized $AuCu_{56}$ NC. Only the Au (pink) and Cu (green) atoms are shown; ligands are omitted for clarity.

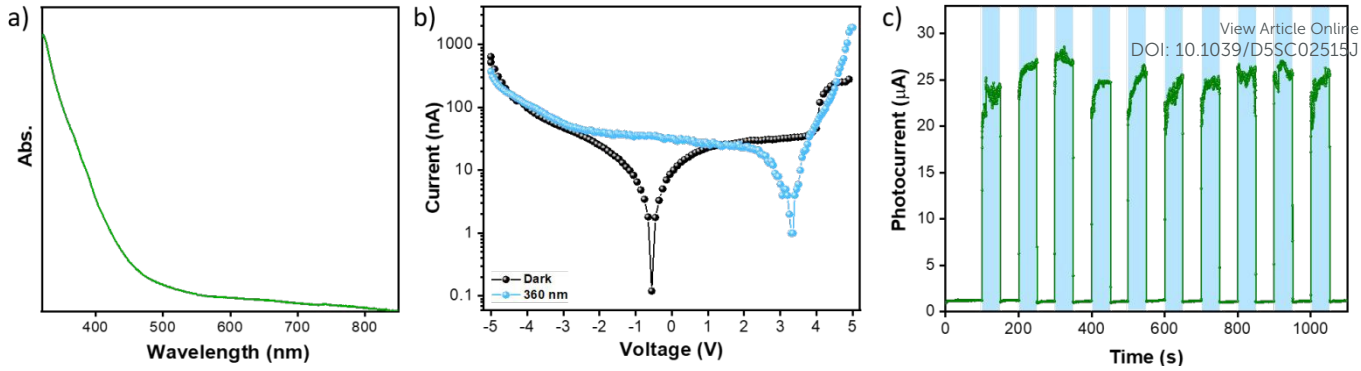


**Figure 5.** a) UV-vis absorption spectrum of the $AuCu_{56}$ crystals dispersed in DCM. b) I-V characteristics of the device in dark and 360 nm of laser illumination. c) Photoresponse of the device under 360 nm laser irradiation, with the arrows indicating the response and recovery time of the device.

**Table S4.** The electrochemical formal potential for the first one-electron oxidation of the NC is only slightly positive. A relatively negative potential is separated from the first oxidation potential by a significant energy gap of 1.17 V in MeCN (**Fig. 3d**). The energy gap comprises work terms linked to the charging of the NC $(AuCu_{56})^+$ and $(AuCu_{56})^-$, commonly termed charging or addition energy.[58] This estimation is derived from the difference between the formal potentials of $(AuCu_{56})^{+/0}$ and $(AuCu_{56})^{2+/1+}$, which is estimated as 0.13 V in MeCN as indicated in **Table S4** (ox2-ox1). A corrected energy of 1.04 eV is derived from the difference, which serves as the electrochemical prediction for HOMO–LUMO gap energy.[59,60] The +2 and +3 oxidation states originate from the metallic core instead of the ligand, like the 3d-Cu shell manifold. These observations are in agreement with DFT calculations. The cyclic voltammogram **(Fig. S14)** is reversible in nature in the wide range of redox window (e.g., -2.0 to + 2.0 V), which suggests even greater stability and redox flexibility and may serve as a plausible electron reservoir.

**Electronic structure analysis.** To further understand the electronic structure of the $AuCu_{56}$ NC, we performed density functional theory (DFT) calculations to first optimize its structure. Then analyze the frontier orbitals and spin density. Both HOMO and LUMO orbitals (**Figs. 4a,b**) were found to show clear superatomic features: the HOMO resembles an S orbital, while LUMO a P orbital. This is fully consistent with the superatom complex theory[6] according to which the $AuCu_{56}$ NC will have only one free electron and a superatomic electron configuration of $1S^1$. While the distribution of HOMO or the 1S orbital concentrates on the central Au, it does extend to the Cu layers. This unpaired electron configuration of the $AuCu_{56}$ NC was further confirmed using electron paramagnetic resonance (EPR) spectroscopic measurements of the NC at 298 K, where a EPR signal with a g-tensor = 2.11 was observed (**Fig. S15**).[61] The superatomic picture is further confirmed by the concentric bond analysis[62] of the $Au@Cu_{14}S_{12}@Cu_{36}$ core of the cluster (**Fig. S16**), which shows a similar orbital concentration on the central Au but extends to the $Cu_{14}$ layer. The atomic charge on the central gold atom was found to be +0.262 from the Mulliken population analysis, suggesting that it loses some fraction of its free electron to the $Cu_{14}$ shell and beyond, consistent with the HOMO in **Fig. 4a**. The LUMO or 1P orbital are mainly located in the Cu layers. This means that there is a very intimate mixing of Au 6s and Cu 4s electrons, beyond a simplified picture of Au-centered Cu NC with the Cu atoms in the +1 state. The spin density distribution reinforces this idea: it is scattered around the center Au atom as well as around many Cu atoms (**Fig. 4c**).

**Photocurrent Response.** The UV-vis absorption spectroscopy of the NC showed a broad absorption below 400 nm (**Fig. 5a**), which is commonly observed in high-nuclearity Cu NCs.[63–66] The onset of the absorption spectrum indicates a low band gap value. Owing to this UV range absorption and low band gap of the $AuCu_{56}$ NC, the photo-response of the sample was studied under UV illumination in a typical two-electrode system using drop-casting method on prefabricated Interdigitated Electrodes (IDE) device over $Si/SiO_2$ substrate with Cr/Au patterned electrodes **(Fig. S17a)**. **Fig 5b** shows the I-V characteristics of the sample in the dark and under the illumination of a 360 nm laser (10 mW). Upon light irradiation, there is a clear change in the current compared to the dark condition, which confirms that the material generates a photocurrent i.e., electron-hole pair generation under the illumination of light. There is a clear offset in I-V characteristics for both dark and light conditions, which can be attributed to heterojunction formation in the sample. Upon applying a bias of 5V through the device, ten on-off cycles with irradiation of 360 nm laser were observed **(Fig. 5c)**. The blue shaded region shows the photoresponse observed under laser illumination. Each on-off cycle shows a constant change in the current, indicating its high stability over each cycle. A significant order of ~20 μA of photocurrent is generated for the 360 nm laser light with 10 mW of power. The device has a good response and recovery time of ~200 ms **(Figs. S17b, c),** comparable to other NC-based materials.[67–71] Due to its broad absorption in the visible region, the photoresponse of the device was also tested with a white light source, which gave a photocurrent response of ~15 μA **(Fig. S18)**. This photocurrent response alongwith the DFT calculations directly link the $1S^1$ superatomic state to the photocurrent generation. The electronic structure analysis (**Figs. 4a, b**) shows that the HOMO is a superatomic 1S orbital and the LUMO is a 1P orbital. Importantly, the HOMO (1S) charge is concentrated at the central Au core while the LUMO (1P) lies on the Cu outer shell.

Thus, photoexcitation moves the unpaired 1S electron from the core into a shell centered 1P level. This core shell shift naturally separates the photoelectron from its hole. Moreover, the spin-density distribution (**Fig. 4c**) shows that it is scattered on the Cu shell with little at Au, demonstrating that excitation produces an electron-hole pair with the electron on the periphery and the hole at the core. This arrangement is essential to yield efficient charge separation in analogous superatomic clusters.[67]
Thus, the $AuCu_{56}$ NC has a good generation and separation efficiency of the photoinduced electron-hole pairs as well as a good electron transport property, leading to a faster generation or decay of the photocurrent under light illumination or dark conditions, respectively.

## Conclusions

In summary, a superatomic $[AuCu_{56}S_{12}(SAdm)_{20}(O_3SAdm)_{12}]$ NC was synthesized from an eight-electron $[Au_{23}(S\text{-}c\text{-}C_6H_{11})_{16}]^-$ NC through a ligand exchange coupled metal-exchange induced transformation. The time-dependent mass spectrometric studies showed the simultaneous occurrence of LEIST and MEIST led to the formation of $AuCu_{56}$ NC. This NC can be viewed as a unique Au-centered double-shell copper framework protected by thiolate ligands. The electronic structure calculations revealed an electronic configuration of $1S^1$ for the superatomic $AuCu_{56}$. The electrochemical studies and the theoretical calculations revealed the low band gap of the material, validating the good photoresponse of the material upon UV irradiation with a good response and recovery time. This unique synthetic strategy allowed us to understand the evolution of the superatomic bimetallic NC and promotes the rational design of metal NCs for future applications.

## Data availability

**Supporting Information** contains experimental details, structural details, MALDI and ESI-MS, TEM, XPS, and CV data and measurement details, theoretical calculation details, crystal structure parameters, selected bond lengths, photo-current data.

## Author contributions

S. G. designed and performed the synthesis, characterization, and data interpretation with the assistance from J. T. and D. V. B. L. and D. J. performed the theoretical calculations. A. K. performed the electrochemical measurements. The photo-current measurements were conducted by D. M. and V. K. S. M. conceived and supervised the project, and was involved in data analysis. All authors were involved in the discussion of results and manuscript writing.

## Conflicts of interest

The authors declare no competing interest.

## Funding Sources

View Article Online
DOI: 10.1039/D5SC02515J

Funding for the project was met from the Science and Engineering Research Board (SERB) through the grants CRG/2022/000984. AK thanks the Science and Engineering Research Board (SERB), Government of India, for a National Post-Doctoral Fellowship (PDF/2023/002916).

DFT computation (BL and DJ) was supported by the U.S. Department of Energy, Office of Science, Office of Basic Energy Sciences, Chemical Sciences, Geosciences, and Bio-sciences Division, Catalysis Science Program.

## References

1 R. Jin, C. Zeng, M. Zhou and Y. Chen, *Chem. Rev.,* 2016, **116**, 10346–10413.

2 Y. Du, H. Sheng, D. Astruc and M. Zhu, *Chem. Rev.,* 2020, **120**, 526–622.

3 I. Chakraborty and T. Pradeep, *Chem. Rev.,* 2017, **117***,* 8208–8271.

4 R. Jin, G. Li, S. Sharma, Y. Li and X. Du, *Chem. Rev.,* 2021, **121**, 567–648.

5 Y.-H. Xu, W.-J. Tian, A. Muñoz-Castro, G. Frenking and Z.-M. Sun, *Science*, 2023, **382**, 840–843.

6 M. Walter, J. Akola, O. Lopez-Acevedo, P. D. Jadzinsky, G. Calero, C. J. Ackerson, R. L. Whetten, H. Grönbeck and H. Häkkinen, *Proc. Natl. Acad. Sci. U. S. A.*, 2008, **105**, 9157–9162.

7 H. Häkkinen, *Chem. Soc. Rev.*, 2008, **37**, 1847.

8 M. Zhu, C. M. Aikens, F. J. Hollander, G. C. Schatz and R. Jin, *J. Am. Chem. Soc.*, 2008, **130**, 5883–5885.

9 M. A. Tofanelli and C. J. Ackerson, *J. Am. Chem. Soc.*, 2012, **134**, 16937–16940.

10 T. Omoda, S. Takano and T. Tsukuda, *Small,* 2021, **17**, 2001439-2001457.

11 C. P. Joshi, M. S. Bootharaju, M. J. Alhilaly and O. M. Bakr, *J. Am. Chem. Soc.*, 2015, **137**, 11578–11581.

12 P. D. Jadzinsky, G. Calero, C. J. Ackerson, D. A. Bushnell and R. D. Kornberg, *Science (1979)*, 2007, **318**, 430–433.

13 H. Häkkinen, M. Walter and H. Grönbeck, *J. Phys. Chem. B*, 2006, **110**, 9927–9931.

14 K. Nunokawa, S. Onaka, M. Ito, M. Horibe, T. Yonezawa, H. Nishihara, T. Ozeki, H. Chiba, S. Watase and M. Nakamoto, *J. Organomet. Chem.*, 2006, **691**, 638–642.

15 C. E. Briant, B. R. C. Theobald, J. W. White, L. K. Bell, D. M. P. Mingos and A. J. Welch, *J. Chem. Soc. Chem. Commun.*, 1981, 201–202.

16 L. C. McKenzie, T. O. Zaikova and J. E. Hutchison, *J. Am. Chem. Soc.*, 2014, **136**, 13426–13435.

17 S. Takano and T. Tsukuda, *J. Am. Chem. Soc.*, 2021, **143**, 1683–1698.

18 H. Yi, S. M. Han, S. Song, M. Kim, E. Sim and D. Lee, *Angew. Chem. Inter. Ed.*, 2021, **60**, 22293–22300.

19 A. Tlahuice-Flores and A. Muñoz-Castro, *Int. J. Quantum Chem.,* 2019, **119**, e25756-e25768.

20 E. Ito, S. Takano, T. Nakamura and T. Tsukuda, *Angew. Chem. Inter. Ed.*, 2021, **60**, 645–649.

21 R. Saito, K. Isozaki, Y. Mizuhata and M. Nakamura, *J. Am. Chem. Soc.*, 2024, **146**, 20930–20936.

22 C. Zeng, Y. Chen, A. Das and R. Jin, *J. Phys. Chem. Lett.,* 2015*,* **6***,* 2976–2986.

23 K. R. Krishnadas, A. Baksi, A. Ghosh, G. Natarajan and T. Pradeep, *Nat. Commun.*, 2016, **7**, 13447.

24 S. Gratious, S. Mukherjee and S. Mandal, *J. Phys. Chem. Lett.*, 2022, **13**, 9014–9027.

25 S. Gratious, E. N. Nahan, R. Jin and S. Mandal, *Acc. Mater. Res.,* 2024, **5**, 1291-1302.

26 X. Kang, Y. Li, M. Zhu and R. Jin, *Chem. Soc. Rev.,* 2020*,***49***,* 6443-6514.

27 X. Kang and M. Zhu, *Chem. Mater.*, 2019, **31**, 9939–9969.

28 Y. Kim, S. Ji and J.-M. Nam, *Acc. Chem. Res.,* **2023,** *56*, 2139–215.

29 C. Zeng, C. Liu, Y. Pei and R. Jin, *ACS Nano*, 2013, **7**, 6138–6145.

30 W. Suzuki, R. Takahata, Y. Chiga, S. Kikkawa, S. Yamazoe, Y. Mizuhata, N. Tokitoh and T. Teranishi, *J. Am. Chem. Soc.*, 2022, **144**, 12310–12320.

31 X. Meng, Q. Xu, S. Wang and M. Zhu, *Nanoscale*, 2012, **4**, 4161.

32 S. Yang, J. Chai, Y. Song, J. Fan, T. Chen, S. Wang, H. Yu, X. Li and M. Zhu, *J. Am. Chem. Soc.*, 2017, **139**, 5668–5671.

33 Q. Li, K. J. Lambright, M. G. Taylor, K. Kirschbaum, T. Y. Luo, J. Zhao, G. Mpourmpakis, S. Mokashi-Punekar, N. L. Rosi and R. Jin, *J. Am. Chem. Soc.*, 2017, **139**, 17779–17782.

34 Y. Negishi, T. Iwai and M. Ide, *Chem. Commun.*, 2010, **46**, 4713.

35 Q. Li, T.-Y. Luo, M. G. Taylor, S. Wang, X. Zhu, Y. Song, G. Mpourmpakis, N. L. Rosi and R. Jin, *Sci Adv.*, 2017, **3**, e1603193-e1603200.

36 S. Wang, Y. Song, S. Jin, X. Liu, J. Zhang, Y. Pei, X. Meng, M. Chen, P. Li and M. Zhu, *J. Am. Chem. Soc.*, 2015, **137**, 4018–4021.

37 M. S. Bootharaju, L. Sinatra and O. M. Bakr, *Nanoscale*, 2016, **8**, 17333–17339.

38 M. Zhu, P. Wang, N. Yan, X. Chai, L. He, Y. Zhao, N. Xia, C. Yao, J. Li, H. Deng, Y. Zhu, Y. Pei and Z. Wu, *Angew. Chem. Inter. Ed.*, 2018, **57**, 4500–4504.

39 N. Xia and Z. Wu, *J. Mater. Chem. C.*2016, **4**, 4125–4128.

40 C. Yao, J. Chen, M. B. Li, L. Liu, J. Yang and Z. Wu, *Nano Lett.*, 2015, **15**, 1281–1287.

41 Z. Wu, *Angew. Chem. Inter. Ed.*, 2012, **51**, 2934–2938.

42 M. S. Bootharaju, C. P. Joshi, M. R. Parida, O. F. Mohammed and O. M. Bakr, *Angew. Chem. Inter. Ed.*, 2016, **55**, 922–926.

43 K. R. Krishnadas, A. Ghosh, A. Baksi, I. Chakraborty, G. Natarajan and T. Pradeep, *J. Am. Chem. Soc.*, 2016, **138**, 140–148.

44 K. R. Krishnadas, A. Baksi, A. Ghosh, G. Natarajan and T. Pradeep, *ACS Nano*, 2017, **11**, 6015–6023.

45 S. Bhat, A. Baksi, S. K. Mudedla, G. Natarajan, V. Subramanian and T. Pradeep, *J. Phys. Chem. Lett.*, 2017, **8**, 2787–2793.

46 M. M. Maman, N. N. E. K, G. Suresh, A. Das, A. S. Nair, B. Pathak, and S. Mandal, *Nanoscale*, 2023, **15,** 13102-13109.

47 S. Gratious, A. Afreen, E. Mahal, J. Thomas, S. Saha, A. S. Nair, K. V. Adarsh, B. Pathak, and S. Mandal, *Chem. Sci.*, 2024, **15**, 9823-9829.

48 N. N. Eyyakkandy, A. Afreen, G. Vilangappurath, S. Gratious, K. V. Adarsh and S. Mandal, *J. Phys. Chem. C*, 2024, **128**, 18828–18835.

49 X. Kang, M. Ren, M. Zhu and K. Zhang, *Chem. Mater.*, 2020, **32**, 6736–6743.

50 Y. Niihori, Y. Kikuchi, A. Kato, M. Matsuzaki and Y. Negishi, *ACS Nano*, 2015, **9**, 9347–9356.

51 A. Das, T. Li, K. Nobusada, C. Zeng, N. L. Rosi and R. Jin, *J. Am. Chem. Soc.*, 2013, **135**, 18264–18267.

52 C. Xu, Y. Jin, H. Fang, H. Zheng, J. C. Carozza, Y. Pan, P.-J. Wei, Z. Zhang, Z. Wei, Z. Zhou and H. Han, *J. Am. Chem. Soc.*, 2023, **145**, 25673–25685.

53 X. Kang, X. Wei, X. Liu, S. Wang, T. Yao, S. Wang and M. Zhu, *Nat. Commun.*, 2021, **12**, 6186.

54 L.-J. Liu, J.-W. Zhang, M. Asad, Z.-Y. Wang, S.-Q. Zang and T. C. W. Mak, *Chem. Commun.*, 2021, **57**, 5586–5589.

55 M. P. Casaletto, A. Longo, A. Martorana, A. Prestianni and A. M. Venezia, *Surf. Interface Anal.,* 2006, **38**, 215–218.

56 A. K. Das, S. Biswas, A. Pal, S. S. Manna, A. Sardar, P. K. Mondal, B. Sahoo, B. Pathak and S. Mandal, *Nanoscale*, 2024, **16**, 3583–3590.

57 Y. Yang and S. Chen, *Nano Lett.*, 2003, **3**, 75–79.

58 C. Creutz, B. S. Brunschwig and N. Sutin, in *Comprehensive Coord. Chem. II*, 2003, **7**, 731–777.

59 Y. Negishi, K. Munakata, W. Ohgake and K. Nobusada, *J. Phys. Chem. Lett.*, 2012, **3**, 2209–2214.

60 D. Lee, R. L. Donkers, G. Wang, A. S. Harper and R. W. Murray, *J. Am. Chem. Soc.*, 2004, **126**, 6193–6199.

61 M. Agrachev, M. Ruzzi, A. Venzo and F. Maran, *Acc. Chem. Res.*, 2019, **52**, 44–52.

62 A. Muñoz-Castro, *ChemPhysChem*, 2025, **26**, e202400892.

63 A. Baghdasaryan and T. Bürgi, *Nanoscale*, 2021, **13**, 6283–6340.

64 B.-L. Han, Z. Liu, L. Feng, Z. Wang, R. K. Gupta, C. M. Aikens, C.-H. Tung and D. Sun, *J. Am. Chem. Soc.*, 2020, **142**, 5834–5841.

65 A. Baghdasaryan, C. Besnard, L. M. Lawson Daku, T. Delgado and T. Burgi, *Inorg. Chem.*, 2020, **59**, 2200–2208.

66 R.-W. Huang, J. Yin, C. Dong, A. Ghosh, M. J. Alhilaly, X. Dong, M. N. Hedhili, E. Abou-Hamad, B. Alamer, S. Nematulloev, Y. Han, O. F. Mohammed and O. M. Bakr, *J. Am. Chem. Soc.*, 2020, **142**, 8696–8705.

67 S. Biswas, A. K. Das, A. C. Reber, S. Biswas, S. Bhandary, V. B. Kamble, S. N. Khanna and S. Mandal, *Nano Lett.*, 2022, **22**, 3721–3727.

68 Z. Wang, L. Li, L. Feng, Z. Gao, C. Tung, L. Zheng and D. Sun, *Angew. Chem. Inter. Ed.* 2022, **61**, 823- 832.

69 Z. Wang, Y.-J. Zhu, B.-L. Han, Y.-Z. Li, C.-H. Tung and D. Sun, *Nat. Commun.*, 2023, **14**, 5295.

70 W.-X. Xie, C.-H. Xue, M. Liu, K. Zhou, H.-H. Gu, J.-Y. Ji, B.-K. Chen, N. Liu and Y.-F. Bi, *Dalton Trans.*, 2023, **52**, 13405–13412.

71 H. Zhao, C. Zhang, B. Han, Z. Wang, Y. Liu, Q. Xue, C.-H. Tung and D. Sun, *Nat. Synth.*, 2024, **3**, 517–526.



View Article Online
DOI: 10.1039/D5SC02515J

## Data availability statement

The data will be available from the authors on request for academic purpose.